Proceedings of OMAE2009
ASME 28th International Conference on Ocean, Offshore and Arctic Engineering
May 31 - June 5, 2009, Honolulu, Hawaii

OMAE2009-79342

DRAFT: CFD SIMULATIONS OF A SEMI-SUBMERSIBLE WITH ABSORBING BOUNDARY CONDITIONS

Peter R. Wellens
Ship Hydromechanics Laboratory
Delft University of Technology
Mekelweg 2, 2628 CD Delft
The Netherlands
Email: P.R.Wellens@tudelft.nl

Roel Luppes
Department of Mathematics
University of Groningen
PO Box 407, 9700 AK Groningen
The Netherlands
Email: r.luppes@math.rug.nl

Arthur E.P. Veldman
Department of Mathematics
University of Groningen
PO Box 407, 9700 AK Groningen
The Netherlands
Email: veldman@math.rug.nl

Mart J.A. Borsboom
Deltares
PO Box 177, 2600 MH Delft
The Netherlands
Email: Mart.Borsboom@deltares.nl

ABSTRACT

The CFD tool COMFLOW *is suitable for simulations of two-phase flows in offshore applications.* COMFLOW *solves the Navier-Stokes equations in both water and (compressible) air. The water surface is advected through a Volume-of-Fluid method, with a height-function approach for improved accuracy.*

By employing Absorbing Boundary Conditions (ABC), boundaries can be located relatively close to an object, without influencing outgoing waves or generating numerical reflections that affect the waves inside the flow domain. Traditionally, boundaries are located far from the obstacle to avoid reflections; even when numerical damping zones are used. Hence, with the ABC approach less grid points are required for the same accuracy, which reduces the computing time considerably.

Simulations of a semi-submersible model are compared to measurements. The overall agreement is reasonably good, for a wide range of wave conditions. The ABC performs well; numerical reflections are almost absent. Moreover, computing times reduce with a factor four compared to damping zone techniques.

INTRODUCTION

During the life time of an offshore structure, it encounters a variety of loading conditions. Operational conditions dominate the design of the structure regarding fatigue and general motion behaviour in the long term. The survival condition can be regarded as the most likely, worst storm a structure can encounter. Critical damage as a result of extreme wave loading needs to be prevented. With experiments, the structure's response in both operational and extreme conditions can be assessed. Numerical simulations beforehand, of the structure in waves, are an important engineering tool in setting up experiments, as they indicate critical loading conditions. Simulations afterwards can help to understand the experimental results.

The industry standard for the simulation of (sub-)harmonic motion behaviour of offshore structures in operational conditions, are linear 3D boundary element methods (BEM) in the frequency domain. With BEMs, long term statistics of the structure's response are easily generated, but their application is restricted to mild seas, because of the assumption of linearity.

In extreme seas, there is the risk of deck impact for semi-submersibles, tension-leg platforms and bottom founded structures. In case of ship-shaped production platforms (FPSOs), green water may flood the deck and impact with topside equipment. Various numerical methods are available for the time-domain simulation of extreme free surface events that result in impact loading. Smoothed particle hydrodynamics (SPH) is a meshless method, in which fluid particles directly exchange momentum within a limited region of influence. In level-set methods, a level-set function, represented by a band of grid cells near the free surface, is used to describe the fluid configuration. In volume-of-fluid (VOF) methods, filling rates of individual cells are administrated. Fluid fragments are advected with local velocities and the free surface position is subsequently reconstructed from combined fluid volumes contained in single cells.

The numerical method COMFLOW is based on the Navier-Stokes equations, in which a VOF method is applied to describe the evolution of the free surface, see e.g. [1–13]. A local height function near the free surface yields improved performance in terms of mass conservation and the number of disconnected droplets, compared to the original VOF method introduced in [14]. COMFLOW intends to simulate extreme wave impact events, as if the structure were out at sea. For reasons of efficiency, the domain should ideally be confined to the direct surroundings of the structure. For an accurate representation of the wave system near the structure, spurious wave reflections from the boundaries of the computational domain need to be prevented. A common approach is to incorporate absorbing layers or numerical damping zones, which require multiple (significant) wave lengths to effectively dissipate wave energy and thus prevent reflections. Especially in 3D, and in case of long waves, this requirement conflicts with our desire to keep the domain size only slightly larger than the structure itself. For this reason, an absorbing boundary condition (ABC) has been developed for the benefit of extreme wave impact simulations with COMFLOW.

This paper presents the derivation of the ABC and the numerical approximation of the analytical operator, which is required for incorporation in the numerical method. The performance of the ABC is tested in actual simulations and compared to the theoretical reflection coefficient and to the performance of a traditional absorbing layer. Before we conclude, the ABC is used in a 3D simulation including a semi-submersible, of which the outcome is validated with experimental results.

GOVERNING EQUATIONS

Since the compressibility of air is important for wave impact simulations, the governing equations for compressible fluid flow are given here, presented in conservation form for a volume Ω with boundary Γ and normal vector $\vec{n}$. In terms of time t, fluid density ρ, velocity vector $\vec{u} = (u,v,w)^T$, pressure p and dynamic viscosity μ, conservation of mass and momentum are given by:

$$\int_\Omega \frac{\partial \rho}{\partial t} d\Omega + \oint_\Gamma (\rho \vec{u}) \cdot \vec{n}\, d\Gamma = 0 \quad (1)$$

$$\int_\Omega \frac{\partial (\rho \vec{u})}{\partial t} d\Omega + \oint_\Gamma \rho \vec{u} \, (\vec{u} \cdot \vec{n}) \, d\Gamma + \oint_\Gamma p \vec{n}\, d\Gamma - \oint_\Gamma \left(\mu \left(\nabla \vec{u} + \nabla \vec{u}^T \right) - \frac{2}{3} \mu \nabla \cdot \vec{u} \right) \cdot \vec{n}\, d\Gamma - \int_\Omega \rho \vec{F}\, d\Omega = 0. \quad (2)$$

In absence of further external loading, the external force $\vec{F}$ consists of gravity only. As described below, an adiabatic relation between pressure and density closes the system of Navier-Stokes equations (1) and (2), see also e.g. [10–13].

A no-slip boundary condition $\vec{u} = 0$ is imposed on the surface of structures. The same boundary condition is used for the domain bottom and domain ceiling. Along the side walls of the domain, ideally, ABCs for waves are applied. Below, an ABC for long-crested, irregular outgoing waves is discussed.

NUMERICAL METHOD

The numerical model has been implemented in the 3D Navier-Stokes solver COMFLOW, in which a VOF method is applied to describe the evolution of the free surface, with a height-function approach for improved accuracy. COMFLOW has been developed initially at the University of Groningen to study the sloshing of liquid on board spacecraft in micro-gravity, for which a very accurate and robust description of the free surface is required [1, 3, 7, 9]. In close cooperation with MARIN (Maritime Research Institute Netherlands), the methodology was extended to simulations of green water loading on a fixed bow deck [4]. Later on, the range of applications has been extended to impact loads on fixed structures [2, 5, 6], anti-roll tanks and sloshing tanks [8, 10–13].

Cell Labeling Method

Every grid cell is given a label to distinguish between fluid, air and boundary. These labels depend on the variables F_b and F_s, which denote the fraction of a grid cell open for fluid and the fraction of a cell filled with the liquid phase, respectively. Two classes of labeling exist: geometry labels and fluid labels. At each time step, geometry labeling divides the cells into three types: **F**low cells (all cells with $F_b > 0$), **B**oundary cells (adjacent to a **F**-cell) and e**X**ternal cells (all remaining cells). The free-surface labeling is a subdivision of the **F**-cells: **E**mpty cells (all cells with $F_s = 0$), **S**urface cells (adjacent to an **E**-cell) and **F'**luid cells (all remaining **F**-cells).

In Fig. 1 an example is shown of geometry and free-surface cell labeling for wave impact (from the right) on a rectangular container. The labeling system stems from a one-phase model, but is retained in the current two-phase model. In one-phase simulations, E-cells are truly empty and are left out of the computations, while free surface boundary conditions are prescribed

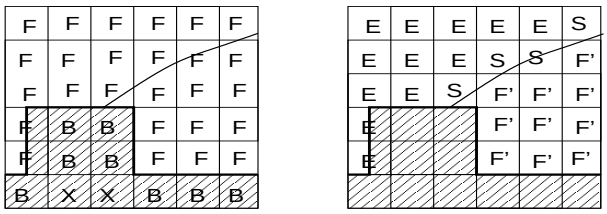

Figure 1: GEOMETRY (LEFT) AND FREE-SURFACE (RIGHT) CELL LABELING FOR WAVE IMPACT ON A RECTANGULAR CONTAINER.

around S-cells. In the two-phase model, E-cells are filled with air and are thus included in the simulation.

Discretisation of the Navier-Stokes Equations

Initially, the Navier-Stokes equations (1) and (2) are discretised in time by means of the first order Forward Euler method:

$$\frac{\rho^{n+1}-\rho^n}{\Delta t}+\rho^n\nabla\cdot\vec{u}^{n+1}+\vec{u}^n\nabla\rho^n=0 \qquad (3)$$

$$\frac{\vec{u}^{n+1}-\vec{u}^n}{\Delta t}+\frac{\vec{u}^n}{\rho^n}\frac{\rho^{n+1}-\rho^n}{\Delta t}+\frac{1}{\rho^n}\nabla\cdot(\rho^n\vec{u}^n\vec{u}^n)+\frac{1}{\rho^n}\nabla p^{n+1} -\frac{1}{\rho^n}\nabla\left(\mu^n\left(\nabla\vec{u}^n+\nabla\vec{u}^{T\,n}\right)-\frac{2}{3}\mu^n\nabla\cdot\vec{u}^n\right)-\vec{F}^n=0, \qquad (4)$$

with n and $n+1$ the old and new time level and Δt the time step. Spatial discretisation is done on a staggered Cartesian grid, with the pressure located in cell centers and the velocity components in the middle of the cell faces between grid cells. The convective term $\frac{1}{\rho^n}\nabla\cdot(\rho^n\vec{u}^n\vec{u}^n)$ in Eqn. (4), which dominates in case of momentum-driven applications, is treated with symmetry preserving spatial discretisation [15]. When the first-order upwind (B2) scheme is applied, only one upstream point is taken into account, whereas the second-order upwind (B3) scheme uses information from two upstream points. The B2 scheme applies a large amount of artificial diffusion to obtain a stable solution, which may lead to an undesirable amount of damping of the fluid motion. Using the second-order upwind (B3) scheme, the applied level of artificial diffusion is smaller, resulting in less damping, but for B3 an alternative time discretisation is needed to generate stable solutions [8, 10–13].

The Forward Euler (FE) method only uses information from the previous time level n to calculate a variable ϕ at level $n+1$, whereas the second-order Adams-Bashforth (AB) method also uses the older time level $n-1$:

$$\phi^{n+1}_{FE}=\phi^n+\Delta t\,f(\phi^n)$$
$$\phi^{n+1}_{AB}=\phi^n+\Delta t\,f(\frac{3}{2}\phi^n-\frac{1}{2}\phi^{n-1})$$

CFL limit η_{max}	*B2 upwind*	*B3 upwind*
Forward Euler	$\eta_{max}\leq 1-d\approx 1$	$\eta_{max}\leq\sqrt{d}\ll 1$
Adams Bashforth	$\eta_{max}\leq\frac{1}{2}-d\approx\frac{1}{2}$	$\eta_{max}\leq\frac{1}{4}-\frac{1}{2}d\approx\frac{1}{4}$

Table 1: CFL LIMIT FOR DIFFERENT SPATIAL UPWIND AND TIME INTEGRATION METHODS.

Both methods are limited in their stability by two quantities: the CFL number $\eta=u\Delta t/\Delta x$ and the diffusion number $d=2\mu\Delta t/(\Delta x)^2$. Apart from the time integration method, the stability limit also depends on the spatial discretisation method applied. In most offshore cases, convection dominates diffusion, and in practice the CFL number η controls the stability limit. In Tab. 1, the limits on the CFL number are summarized for both methods in combination with the two upwind schemes. FE allows a larger time step than AB when the B2 scheme is used. For the B3 scheme, FE is less suitable, while AB allows a larger time step. The lower stability limit for the B3 upwind scheme seems to be a major disadvantage. However, the B3 scheme is needed in situations where the B2 scheme results in an undesired amount of damping of fluid motion due to artificial viscosity [12, 13].

Solving the Pressure

The pressure is calculated by means of a Poisson equation, which is formulated by taking the divergence of the momentum equation (4). The term $\nabla\cdot\vec{u}^{n+1}$ is then substituted into continuity equation (3) to acquire the pressure Poisson equation:

$$\Delta t\nabla\cdot\left(\frac{1}{\rho^n}\nabla p^{n+1}\right)=\frac{1}{\rho^n}\frac{\rho^{n+1}-\rho^n}{\Delta t}+\frac{\vec{u}^n}{\rho^n}\cdot\nabla\rho^n+\nabla\cdot\tilde{\vec{u}}^n, \qquad (5)$$

where $\tilde{\vec{u}}$ denotes an 'intermediate' velocity, which includes convective, diffusive and force effects. Eqn. (5) contains ρ^{n+1}, which is reformulated through an equation of state. The treatment of this term, in combination with the density gradient term, requires more attention and has been described in [12, 13]. The pressure Poisson equation finally reduces to

$$\Delta t\nabla\cdot\left(\frac{1}{\rho^n}\nabla p^{n+1}\right)=\frac{F^n_b-F^n_s}{F^n_b\rho^n}\left(\frac{\rho^{n+1}_g-\rho^n_g}{\Delta t}+\vec{u}^n\nabla\rho^n_g\right)+\nabla\cdot\tilde{\vec{u}}^n. \qquad (6)$$

The derivatives of the density in Eqn. (6) no longer contain large jumps, as they are only determined by the compression and expansion of the gas phase. The gas density ρ_g in (6) is substituted using the polytropic equation of state, in terms of the atmospheric pressure $p_{g,0}$ and ambient gas density $\rho_{g,0}$

$$\frac{\rho^{n+1}_g}{\rho_{g,0}}=\left(\frac{p^{n+1}_g}{p_{g,0}}\right)^{1/\gamma}, \qquad (7)$$

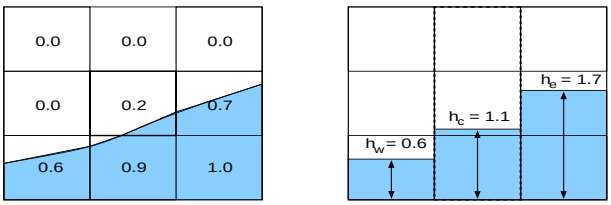

Figure 2: CONSTRUCTION OF THE LOCAL HEIGHT FUNCTION IN A 3X3 BLOCK FOR A CENTRAL S-CELL.

with γ=1.4 for pure air. After substitution in Eqn. (6), the density is linearized by a Newton approximation and transferred to the left-hand side of the Poisson equation, see e.g. [12, 13].

Free Surface Description

The free surface is described by the equation $F_s(\vec{x},t) = 0$, and its motion is described by

$$\frac{DF_s}{Dt} = \frac{\partial F_s}{\partial t} + \vec{u}\cdot\nabla F_s = 0 \tag{8}$$

The free surface displacement is done in two steps. First the free surface is reconstructed and then it is advected to the new position. The reconstruction is done with Simple Linear Interface Calculation (SLIC), where the interface consists of line segments that are constructed parallel or perpendicular to the major flow axes [14]. A characteristic drawback of SLIC is the unphysical creation of flotsam ('floating wreckage') and jetsam ('jettisoned goods'). These terms are used for disconnected isolated droplets that are a result of errors induced by the free surface reconstruction. Moreover, in the original VOF method values are rounded off at the end of the displacement algorithm ($0 \leq F_s \leq 1$), leading to significant losses in liquid mass.

To prevent from isolated droplets and mass losses, a local height function (LHF) has been introduced [1–3, 7, 8]. The LHF is applied in a $3\times3(\times3)$ block (in 2D or 3D) of cells surrounding a central S-cell. First, the orientation of the free surface is determined (horizontal or vertical), depending on F_s values in the surrounding block of cells. Next, the horizontal or vertical height in each row or column is computed by summing the F_s values (see Fig. 2). Based on the LHF, fluid is transported from one cell (donor) to another (acceptor), depending on the magnitude of velocity, time step and grid sizes. The free-surface at the new time instant is then reconstructed by means of another LHF. Compared to the original VOF method [14], the LHF approach results in significantly less droplets and water loss [1, 2]. An alternative method, which is however more difficult to implement, is proposed in [16]. Comparison in [2] learns that for certain flow applications slightly better results can be obtained. However, for the wave-impact simulations considered in this study, the present LHF-method leads to satisfactory results.

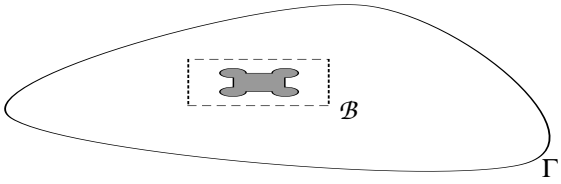

Figure 3: THE NATURAL AND ARTIFICIAL BOUNDARY.

Density at the Free Surface

Attention should be paid to the discretisation of the density in a cell, as it can vary up to factor of 1000. For compressible two-phase flow, the density in the cell center is calculated as

$$\rho = \frac{F_s}{F_b}\rho_l + \frac{(F_b - F_s)}{F_b}\rho_g, \tag{9}$$

where ρ_g is a function of the pressure p located in cell centers. Because of the staggered variable arrangement, ρ is needed at cell edges as well. This a major point of attention, as spurious velocities may be generated due to an inconsistent averaging method. By employing a so-called gravity-consistent method, these spurious velocities are avoided, see e.g. [12, 13].

INCOMING AND OUTGOING WAVES

Since the sea is without end, simulations of sea surface waves near offshore structures need to be performed on unbounded domains or domains with natural boundary conditions on Γ, far away from the structure. For efficiency reasons, the domain is truncated by an artificial boundary $\mathcal{B}$, see Fig. 3. The size of the domain enclosed by $\mathcal{B}$ is preferably limited to the order of the length of the structure. Boundary $\mathcal{B}$ divides the sea in a near-field domain close to the structure, and a far-field domain. It is *artificial*; it has to be modelled as if there were no transition between near and far-field. Boundary $\mathcal{B}$ should be fully open to flow, i.e. waves are allowed to flow into and/or leave the domain at $\mathcal{B}$ without any disturbance. Open boundaries are obtained by imposing boundary conditions that simulate wave behaviour.

Wave Generation

It is fairly straightforward to send waves into the near-field domain. Far-field wave behaviour can be modelled by analytical theory or by an external numerical method that efficiently simulates wave propagation over long distances. The velocities obtained from the far-field methods are then imposed as a boundary condition on the near-field domain, see Fig. 4. If analytical velocity profiles are imposed at the boundary, only little spurious waves are generated.

For wave generation, linear potential theory can be used, but this gives inaccurate kinematics and phase relations in steeper

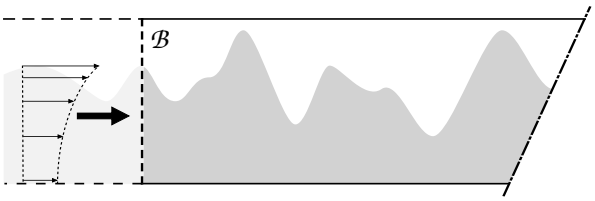

Figure 4: WAVE GENERATION IN NUMERICAL DOMAIN.

waves. For steep long crested regular waves, often used in both experiments and numerical simulations, non-linear stream function theory is available. A system of non-linear equations is formulated by Rienecker and Fenton [17], in which the combination of several harmonic base modes is fitted to kinematic and dynamic free surface boundary conditions. The system is solved by Newton's method. The only approximation is the truncation of the number of base modes.

There is no analytical theory for steep irregular waves. To simulate long-crested steep irregular waves in near-field domains, we use kinematics obtained from an external potential flow method FDFEM [18, 19], a free surface conforming finite element method (FEM) that solves for potential values. Velocities required for the free surface boundary condition are obtained by finite difference (FD) of potential values at the element nodes.

Simulations with regular and irregular waves have been performed to investigate how well steep waves can be represented with COMFLOW. Non-linear effects are significant in steep waves in shallow water. A very long 2D domain is used, which prevents reflected waves at the boundary from interfering with the results. The water depth, wave period, height and length of the regular waves were $d = 10m$, $T = 6s$, $H = 4m$ and $\lambda \approx 50m$, respectively. Different grid resolutions were used, with 50, 100 and 200 cells per wave length and an aspect ratio $a = 1$. The surface elevations ζ, obtained after 24 periods in the regular wave simulations, are presented in Fig. 5. Compared to the analytical Rienecker-Fenton (RF) solution, steep waves in shallow water can be simulated reasonably well when a large number of grid cells is used. Note that the grid resolutions in the legend are for the entire domain. A similar experiment has been performed for irregular waves in a domain of the same size. A JONSWAP spectrum was used with peak period $T_p = 6s$ and significant wave height $H_s = 4m$. In Fig. 6, the free surface after 13 peak periods is shown, starting at $x = 200$. In comparison with the reference solution obtained with the non-linear potential method FDFEM, the longer wave components are represented quite well, but for the shorter components the grid resolution is still too coarse.

Wave Absorption

The far field wave kinematics could also be used for the absorption of outgoing waves if they were known in advance. In

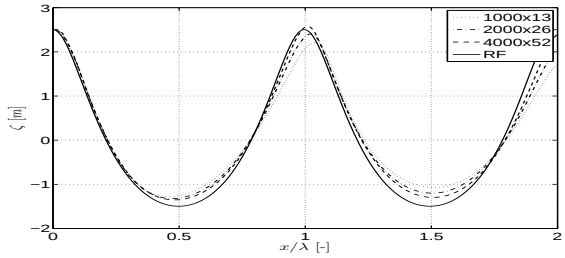

Figure 5: REGULAR WAVE: FREE SURFACE AT $T = 144S$ (2 WAVE LENGTHS). SIMULATIONS ON DIFFERENT GRIDS COMPARED TO THE RF ANALYTICAL SOLUTION.

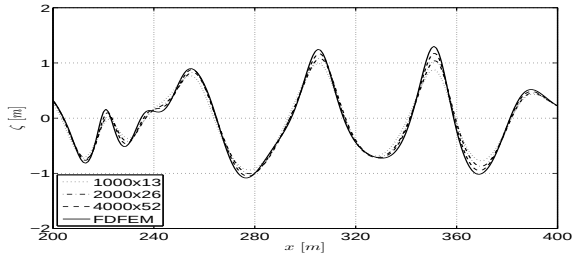

Figure 6: IRREGULAR WAVE: FREE SURFACE AT $T = 98S$. SIMULATIONS ON DIFFERENT GRIDS COMPARED TO THE FDFEM REFERENCE SOLUTION.

our near-field simulations, however, there is always a structure inside the domain that diffracts and radiates waves away from the structure toward the domain boundaries. The kinematics from diffracted and radiated waves in the near-field domain cannot be anticipated in far-field computations. As a consequence, they will reflect from the domain boundaries.

Absorbing layers or dissipation zones, such as the pressure damping zone presented in [20], can be employed to prevent wave reflections. In pressure damping zones, an additional free surface pressure p_s is used, proportional to the vertical velocity w at the free surface, which counteracts wave motion. Its effect is increased slowly from the beginning of the dissipation zone toward the end of the domain, to prevent wave reflection from the dissipation zone itself:

$$p_s = \alpha(x)\, w(x,t)|_S\,, \tag{10}$$

where α denotes the (variable) dissipation coefficient. In long waves, $w \approx 0$ and hence this pressure damping will not be very effective. In that case, large dissipation zones are required, which however significantly add to the domain size and hence to the computational effort. For reasons of efficiency, we have developed an absorbing boundary condition (ABC), that gives less reflection, especially for long waves, but does not add to the domain size.

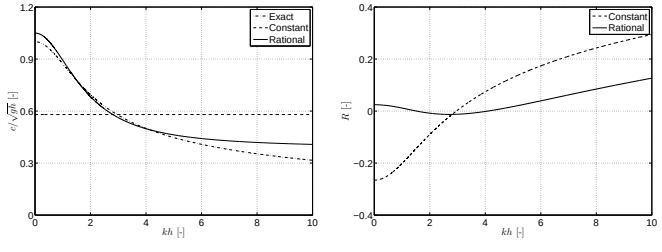

Figure 7: TWO APPROXIMATIONS OF THE DISPERSION RELATION (LEFT) AND THEIR REFLECTION COEFFICIENTS (RIGHT).

ABSORBING BOUNDARY CONDITION (ABC)

The derivation of our ABC starts with the first order Higdon ($\mathcal{H}^{(1)}$) condition

$$\left(\frac{\partial}{\partial t}+c^{out}\frac{\partial}{\partial x}\right)\Phi^{out}=0, \tag{11}$$

where c^{out} is the phase velocity of an outgoing wave component, propagating in positive x-direction. Equation (11), formulated as operator times the potential function Φ, is also known as the Sommerfeld condition. It is perfectly absorbing for this single wave component, but gives more reflection for wave components with other phase velocities. The reflection coefficient is given by:

$$R=\frac{c^{out}-c(kh)}{c^{out}+c(kh)}, \tag{12}$$

in which $c(kh)$ is the true phase velocity of the wave component arriving at the boundary.

The reflection of the ABC for all wave components can be reduced by one order of magnitude, when the condition is expanded to second order ($\mathcal{H}^{(2)}$):

$$\prod_{j=1}^{2}\left(\frac{\partial}{\partial t}+c_j\frac{\partial}{\partial x}\right)\Phi=0. \tag{13}$$

The boundary condition operator now contains higher derivatives in time and in normal direction to the boundary. Spatial derivatives need to be implemented as one sided numerical operators, which may adversely affect the stability of the system [21]. Higher derivatives in time are also undesirable: when the CFL number $\eta\approx 1$, cells that were empty at one moment in time, may become filled during the next time step. In these cells, higher time derivatives cannot be resolved, because insufficient information from the past is available.

Here we follow an alternative approach, inspired by [22] and [23]. Consider the fact that the constant function $c=c^{out}$ is actually a poor approximation of the true (linear) dispersion relation, given by:

$$c=\sqrt{gh}\sqrt{\frac{\tanh(kh)}{kh}}, \tag{14}$$

where $\sqrt{gh}$ is the shallow water phase velocity limit and kh is the dimensionless wave number. Unfortunately, Eqn. (14) cannot be substituted into Eqn. (11), as it cannot be formulated in terms of differential operators. Therefore, the following rational approximation of the dispersion relation (14) is introduced:

$$c_a\approx\sqrt{gh}\frac{a_0+a_1(kh)^2}{1+b_1(kh)^2}, \tag{15}$$

where the coefficients a_0, a_1 and b_1 are chosen such that (14) is approximated well over the largest possible range of kh-values. The Sommerfeld (constant) and rational function approximation of the dispersion relation are shown in Fig. 7(a).

Due to the exponential behaviour (e^{-kz}) of the Φ-values in vertical z-direction, the wave number in Eqn. (15) can be replaced by second derivatives *along* the boundary:

$$k^2\Phi^{out}=\frac{\partial^2}{\partial z^2}\Phi^{out} \tag{16}$$

Combination of Eqns. (11), (15) and (16) yields the formulation of the ABC for dispersive waves:

$$\left[\left(1+b_1h^2\frac{\partial^2}{\partial z^2}\right)\frac{\partial}{\partial t}+\sqrt{gh}\left(a_0+a_1h^2\frac{\partial^2}{\partial z^2}\right)\frac{\partial}{\partial x}\right]\Phi^{out}=0 \tag{17}$$

In Fig. 7(b), the reflection coefficient of Eqn. (17) is given for a range of wave components. Compared to the constant (Sommerfeld) approximation, the reflection coefficient of the rational approximation is smaller over a wide range of values for kh.

Numerical Implementation

The analytical formulation of the ABC has to be approximated numerically for implementation in COMFLOW. It will be implemented at the boundary, which is chosen to coincide with the x-position of the horizontal velocity u in a cell, see Fig. 8. The time derivative of the potential in Eqn. (17) is formally replaced by the pressure according to the linearized Bernoulli equation $\partial\Phi/\partial t=-p-gz$. The spatial derivative normal to the boundary is replaced by the horizontal velocity, i.e. $\partial\Phi/\partial x=u$. To prevent phase differences and resulting spurious reflections, the pressure p in the ABC is evaluated exactly on the boundary, at the same x-position as u. As the solution variables are staggered inside cells, interpolation of the pressure over the boundary is required and a mirror cell for the pressure is introduced, see Fig. 8.

The velocity and the pressure need to be evaluated at the same spatial position, but also at the same moment in time t^{n+1}. The momentum equation is used to eliminate the velocity at the new time instant u_{n+1}:

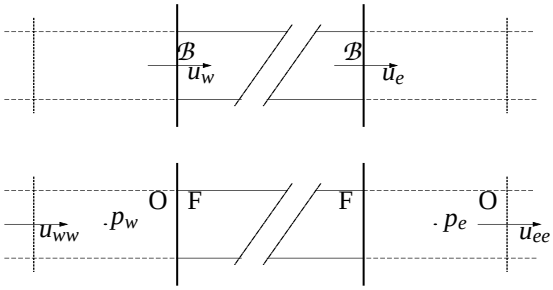

Figure 8: TOP: DOMAIN BOUNDARIES AT THE LEFT AND RIGHT SIDE COINCIDE WITH x-LOCATIONS OF u. BOTTOM: FOR INTERPOLATION OF p EXACTLY ON THE BOUNDARIES, MIRROR CELLS (LABELED WITH O) ARE INTRODUCED CONTAINING p_w and p_e.

$$u_b^{n+1} = u_{i-1}^{n+1} = \tilde{u}_{i-1} - \frac{\Delta t}{\Delta x}\left(p_i - p_{i-1}\right)^{n+1}. \qquad (18)$$

Note that $\tilde{u}$ contains the effect of convection and diffusion, as discussed above. The vertical derivatives in Eqn. (17) are approximated by a numerical operator $\mathcal{V}$ for the second derivative. The following vectors for the horizontal velocity and pressure are introduced:

$$\vec{\tilde{u}} = \left(\tilde{u}_{k-1}\ \ \tilde{u}_k\ \ \tilde{u}_{k+1}\right)^T, \qquad \vec{p} = \left(p_{k-1}\ \ p_k\ \ p_{k+1}\right)^T \qquad (19)$$

Combining (18) and (19) yields the discrete version of the ABC:

$$\left(\mathcal{C}_{lz}\ \ \mathcal{C}_{xl}\ \ \mathcal{C}_{ln}\right)\vec{p}_{i-1} + \left(\mathcal{C}_{zl}\ \ \mathcal{C}_c\ \ \mathcal{C}_{zr}\right)\vec{p}_i = g z_p + \mathcal{R}\vec{\tilde{u}}_{i-1}. \qquad (20)$$

In Eqn. (20), the matrix coefficients $\mathcal{C}$ and right-hand side vector $\mathcal{R}$ are equal to:

$$\begin{array}{ll} \mathcal{C}_{lz} = (-\chi\tau + \frac{1}{2}\psi)\mathcal{V}_1 & \mathcal{C}_{zl} = (\chi\tau + \frac{1}{2}\psi)\mathcal{V}_1 \\ \mathcal{C}_{xl} = -\varphi\tau + \frac{1}{2} - (\chi\tau - \frac{1}{2}\psi)\mathcal{V}_2 & \mathcal{C}_c = \varphi\tau + \frac{1}{2} + (\chi\tau + \frac{1}{2}\psi)\mathcal{V}_2 \\ \mathcal{C}_{ln} = (-\chi\tau + \frac{1}{2}\psi)\mathcal{V}_3 & \mathcal{C}_{zr} = (\chi\tau + \frac{1}{2}\psi)\mathcal{V}_3 \end{array}$$

$$\mathcal{R} = (\chi\mathcal{V}_1 \quad \varphi - \chi\mathcal{V}_2 \quad \chi\mathcal{V}_3),$$

in which: $\varphi = \sqrt{gh}a_0$, $\chi = \sqrt{gh}a_1h^2$, $\psi = b_1h^2$ and $\tau = \Delta t/\Delta x$.

The discrete ABC (20) is essentially an equation for $p_{i,k}$ in a mirror cell outside the domain. On the left-hand side, it only features pressures at the new time level t^{n+1}. The other side has horizontal velocities at time level t^n, stemming from convective and diffusive terms. In Fig. 9 the stencil of pressures is shown for the discrete boundary condition operator and the position of the matrix coefficients in Eqn. (20). The structure of the discrete ABC bears great resemblance to the pressure Poisson equation derived above and can therefore easily be combined with the field equations for the inside of the domain.

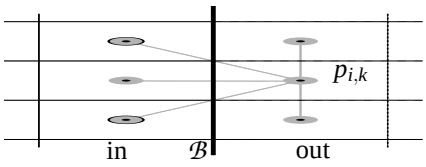

Figure 9: PRESSURE STENCIL AT THE BOUNDARY TO DETERMINE p_i BY MEANS OF THE ABC.

Numerical Performance

The performance of the ABC has been investigated, by comparing the free surface at a specific position in two simulations with different domains. A very long domain is considered, where the surface elevation at the measurement position ($x_m = 200m$) cannot be disturbed by reflections, and a much shorter domain (length $400m$) with ABC at the boundary, see Fig. 10. The water depth in both domains is $d = 100m$. The grid resolution is $\Delta x \times \Delta z = 1m \times 0.5m$, with 5% vertical stretching. A JONSWAP spectrum of irregular waves (wave height $H_s = 4m$, peak period $T_p = 15s$) is simulated during $600s$. The imposed and simulated spectra at the measurement position x_m are shown in Fig. 11. Everything but the boundary condition being the same, any difference can only be attributed to reflection of the ABC.

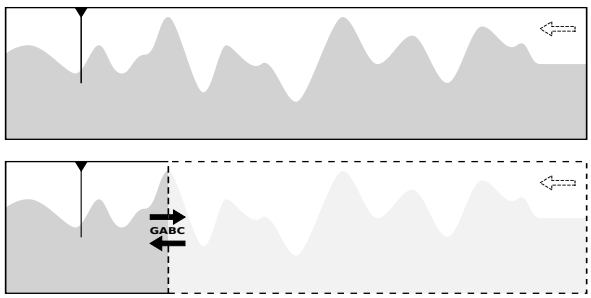

Figure 10: TWO SIMULATIONS: A LONG DOMAIN AND A SHORT DOMAIN WITH ABC. SURFACE ELEVATIONS AT THE INDICATED POSITION DETERMINE REFLECTIONS.

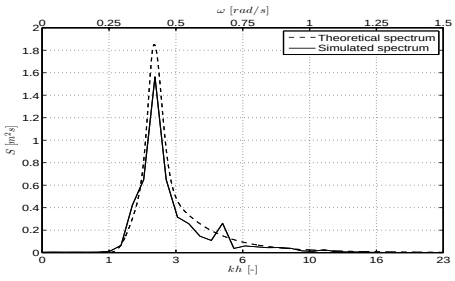

Figure 11: THEORETICAL AND SIMULATED JONSWAP SPECTRUM AT MEASUREMENT POSITION ($x_m = 200m$).

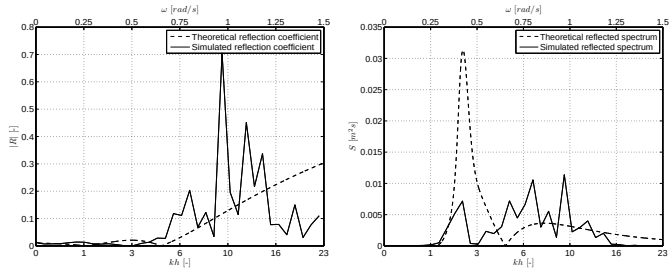

(a) R:ABC (b) S:ABC

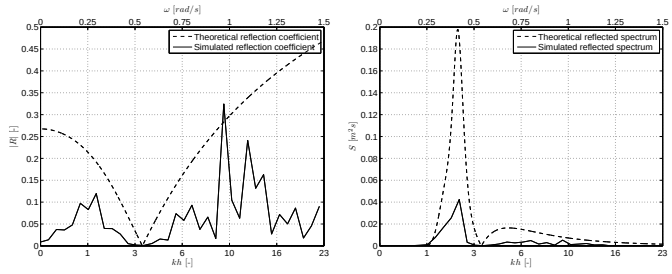

(c) R:Sommerfeld (d) S:Sommerfeld

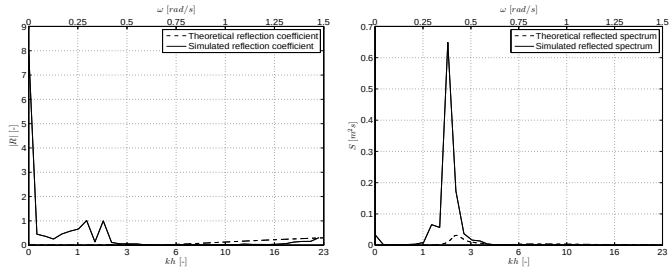

(e) R:dissipation zone (f) S:dissipation zone

Figure 12: THE REFLECTION COEFFICIENTS (a,c,e) AND SPECTRA (b,d,f) OBTAINED WITH ABC, SOMMERFELD AND DISSIPATION ZONE.

Time traces for the reflected waves are obtained by subtracting the surface elevation at x_m in the long domain, from that at x_m in the short domain. These time traces are converted to reflection spectra and reflection coefficients, as shown in Fig. 12(a-d). The ABC has been compared to the theoretical reflection coefficient (12) and to the reflection coefficient of the Sommerfeld equation. The performance of the ABC is generally better than the Sommerfeld condition and accords well with theory. The results do seem to show that the ABC does not perform well for the shorter components, but please note that these components are not represented well on the grid. Moreover, very little wave energy resides at these frequencies, which may adversely influence the results.

The simulation with ABC has also been compared to a simulation where a pressure damping zone is applied, with dissipation coefficient $\alpha = 0.05$ in Eqn. (10). The domain was chosen 3 times as long as the domain with ABC ($3 \times 400 = 1200m$). The

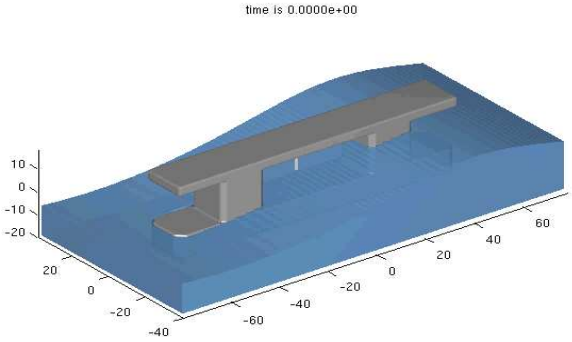

Figure 13: THE SEMI-SUBMERSIBLE MODEL IN THE EXPERIMENT AND A VISUALIZATION OF THE INITIAL CONDITION OF THE NUMERICAL SIMULATION.

theoretical reflection for this configuration is 2% for wave components near the peak frequency of the spectrum. The numerically obtained reflection was 100%. Hence, the dissipation zone is not very well suited for these wave components. The results in Fig. 12(e-f) also show that very long wave components are generated due to non-linear effects in the dissipation zone.

VALIDATED RESULTS

The 1:50 model of the semi-submersible consists of two columns and a pontoon under water, see Fig. 13. At full scale, the pontoon measures $l \times w \times h = 114.5m \times 17.5m \times 10m$. The column width is $17.5m$ and they are $43.5m$ apart. The total draft is $16m$ and the air gap $12m$. The model was kept restrained during the experiments, as a restrained model gives the largest amount of diffraction and run-up of water on the columns. Deck impacts are almost guaranteed, which is highly undesirable for an actual design, but gives the best circumstances for validation of the numerical model. The experiments were performed in a very long, but quite narrow wave basin of $180m$ deep. Waves were generated with a pivoting wave board at one of the narrow ends of the tank. At the opposing end a beach was present to induce wave breaking and prevent reflection. The model was placed a considerable distance away from the wave board.

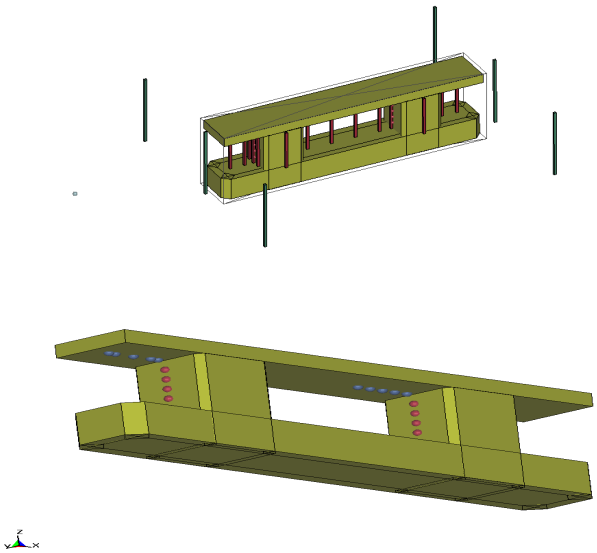

Figure 14: POSITIONS OF THE SENSORS FOR SURFACE ELEVATION (TOP) AND PRESSURE (BOTTOM).

During the experiment, surface elevations were measured around and in between columns and at some distance away from the structure. The columns and the deck were equipped with pressure transducers to monitor the build-up of pressure during a wave impact. In Fig. 14, the positions of the pressure and wave-height sensors are shown. Several sea states were created: regular long crested waves of different periods and wave heights, as well as a number of irregular long crested waves. The regular wave experiment ($H = 15m$ and $T = 11s$) is considered below.

A simulation of the entire wave basin with enough accuracy is not possible on a desktop PC; the domain has to be truncated to the direct surroundings of the structure. The upstream end of the domain is located half a (significant) wave length in front of the structure. The waves will propagate from here to the downstream end, located half a wave length behind the structure. At the ends, potential theory is used to generate waves and the ABC is used to absorb outgoing waves. In accordance with the experiment, the side walls of the domain are fully reflecting and positioned at the location of the side wall of the basin ($y = -100m$ and $y = 100m$).

The simulations have been performed with two different water depths: in case A and B the water depth was equal to $90m$ to save computation time, which is half of the true depth. Case D is a simulation with the full water depth. Different (uniform) grid resolutions were used for the different cases: $\Delta x, y, z = 0.8m$ (case A) and $\Delta x, y, z = 0.5m$ (case B and case D). The results of the simulations are compared to measured signals. In Fig. 15, the wave height between the columns and the run-up on the 2nd column of the semi-submersible are shown. In Fig. 16, the pressure at two locations on the first column are shown: one near the

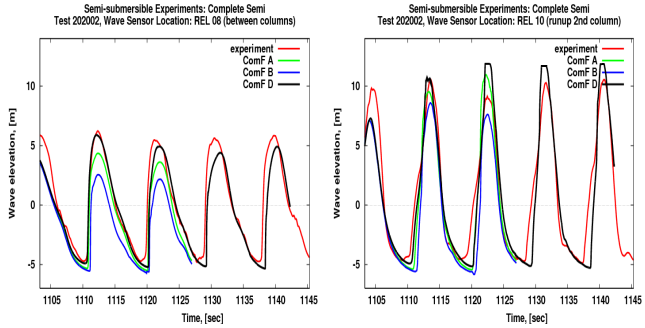

Figure 15: WAVE HEIGHT BETWEEN THE COLUMNS (LEFT) AND RUN-UP ON THE 2ND COLUMN (RIGHT).

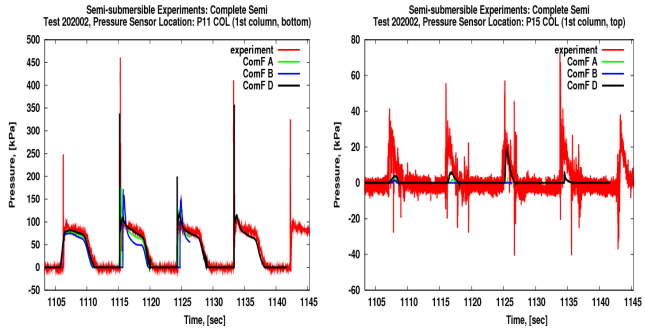

Figure 16: PRESSURE ON THE FIRST COLUMN, NEAR THE PONTOON (LEFT) AND NEAR THE DECK (RIGHT).

pontoon and the other near the deck. In case of the best grid resolution, the agreement with the experiment is generally good. The surface elevation near the columns is well represented and the pressure on the upstream column near the pontoon is very close to measured pressure. The pressure near the deck is slightly underpredicted.

CONCLUSION

The numerical method COMFLOW is suitable for the simulation of two-phase flow in extreme wave impact events, where the free surface may assume any shape. The method can accurately simulate the propagation of both regular and irregular waves, although the required grid resolution is quite demanding.

The numerical method has been combined with a novel Absorbing Boundary Condition (ABC) for long crested dispersive waves. The boundary condition consists of the Sommerfeld condition, combined with a rational approximation of the true linear dispersion relation and vertical derivatives along the boundary.

In numerical simulations of irregular waves, the ABC performs in accordance with the theoretical reflection coefficient. For irregular waves, it gives less reflection than the Sommerfeld

condition and also less reflection than a traditional dissipation zone that was three times as long as the domain with ABC. In comparison with the dissipation zone, we have obtained less reflection, in combination with a reduction of the computational effort of roughly a factor four.

The ABC has been applied in 3D numerical simulations of wave impacts on a semi-submersible model. Surface elevations close to and pressures on the semi-submersible have been compared to experimental results. The overall agreement between simulations and experiments is good. Near the deck, however, the impact pressure is slightly underpredicted.

ACKNOWLEDGMENT

This research is supported by the Dutch Technology Foundation STW, applied science division of NWO and the technology programme of the Ministry of Economic Affairs (#06433). We kindly thank the Maritime Research Institute Netherlands (MARIN) for the experimental results and FORCE Technology in Norway for processing the simulation data.

REFERENCES

[1] Veldman, A.E.P., Gerrits, J., Luppes, R., Helder, J.A. and Vreeburg, J.P.B., 2007. "The Numerical Simulation of Liquid Sloshing On Board Spacecraft". *J. Comp. Phys.*, **224**, pp. 82–99.

[2] Kleefsman, K.M.T., Fekken, G., Veldman, A.E.P., Iwanowski, B. and Buchner, B., 2005. "A Volume-Of-Fluid Based Simulation Method for Wave Impact Problems". *J. Comp. Phys.*, **206(1)**, pp. 363–393.

[3] Gerrits, J. and Veldman, A.E.P., 2003. "Dynamics of Liquid-Filled Spacecraft". *J. Eng. Math.*, **45**, pp. 21–38.

[4] Kleefsman, K.M.T., Fekken, G., Veldman, A.E.P., Buchner, B., Bunnik, T. and Iwanowski, B., 2002. "Prediction of green water and wave loading using a Navier-Stokes based simulation tool". In 21st Int. Conf. OMAE2002-28480.

[5] Kleefsman, K.M.T., Veldman, A.E.P. and Bunnik, T., 2004. "An improved Volume-Of-Fluid (IVOF) method for wave impact type problems". In Spec. Symp. on FPSO Integrity. OMAE-FPSO04-0066.

[6] Kleefsman, K.M.T., Loots, G.E., Veldman, A.E.P., Buchner, B., Bunnik, T. and Falkenberg, E., 2005. "The numerical solution of green water loading including vessel motions and the incoming wave field". In 24th Int. Conf. OMAE2005-67448.

[7] Luppes, R., Helder, J.A. and Veldman, A.E.P., 2006. "The numerical simulation of liquid sloshing in microgravity". In Eur. Conf., ECCOMAS CFD. paper490.

[8] Luppes, R., Wemmenhove, R., Veldman, A.E.P. and Bunnik, T., 2008. "Compressible Two-Phase Flow in Sloshing Tanks". In 5th Eur. Congr., ECCOMAS.

[9] Veldman, A.E.P., 2006. "The simulation of violent free-surface dynamics at sea and in space". In Eur. Conf., ECCOMAS CFD. paper 492.

[10] Wemmenhove, R., Loots, G.E., Luppes, R. and Veldman, A.E.P., 2005. "Modeling two-phase flow with offshore applications". In 24th Int. Conf. OMAE2005-67460.

[11] Wemmenhove, R., Loots, G.E. and Veldman, A.E.P., 2006. "Hydrodynamic wave loading on offshore structures simulated by a two-phase flow model". In 25th Int. Conf. OMAE2006-92253.

[12] Wemmenhove, R., Luppes, R., Veldman, A.E.P. and Bunnik, T., 2007. "Numerical Simulation of Sloshing in LNG Tanks with a Compressible Two-Phase Model". In 26th Int. Conf. OMAE2007-29294.

[13] Wemmenhove, R., Luppes, R., Veldman, A.E.P. and Bunnik, T., 2008. "Application of a VOF Method to Model Compressible Two-Phase Flow in Sloshing Tanks". In 27th Int. Conf. OMAE2008-57254.

[14] Hirt, C.R. and Nichols, B.D., 1981. "Volume Of Fluid (VOF) Method for the Dynamics of Free Boundaries". *J. Comp. Phys.*, **39**, pp. 201–225.

[15] Verstappen, R.W.C.P. and Veldman, A.E.P., 2003. "Symmetry-Preserving Discretisation of Turbulent Flow". *J. Comp. Phys.*, **187**, pp. 343–368.

[16] Youngs, D.L., 1982. "Time-dependent multi-material flow with large fluid distortion". In *Numerical Methods for Fluid Dynamics*, K. W. Morton and M. J. Baine, eds. Academic Press, New York, pp. 273–285.

[17] Rienecker, M.M. and Fenton, J.D., 1981. "A Fourier Approximation Method for Steady Water-Waves". *J. Fluid Mech.*, **104**, pp. 119–137.

[18] Westhuis, J.H., 2001. "The Numerical Simulation of Nonlinear Waves in a Hydrodynamic Model Test Basin". PhD thesis, University of Twente, Netherlands.

[19] van Groesen, E. and Westhuis, J.H., 2002. "Modelling and Simulation of Surface Water Waves". *Math. and Computers in Simulation*, **59**(4), pp. 341–360.

[20] Westhuis, J.H., 2000. "Approximate analytic solutions and numerical wave tank results for the reflection coefficients of a class of numerical beaches". In 10th Int. Conf., pp. 245–252. ISOPE 2000.

[21] Givoli, D. and Neta, B., 2003. "High-Order Nonreflecting Boundary Conditions for the Dispersive Shallow Water Equations". *J. Comput. and Appl. Math.*, **158**(1), pp. 49–60.

[22] Engquist, B. and Majda, A., 1977. "Absorbing Boundary-Conditions for Numerical-Simulation of Waves". *Math. of Comput.*, **31**, pp. 629–651.

[23] Dgaygui, K. and Joly, P., 1994. "Absorbing Boundary-Conditions for Linear Gravity-Waves". *Siam J. Appl. Math.*, **54**(1), pp. 93–131.